

# Interfacial Shear Rheology without an Interfacial Geometry

Iain Muntz<sup>1,2</sup> and Job H. J. Thijssen<sup>1, a)</sup>

<sup>1)</sup> SUPA School of Physics and Astronomy,  
The University of Edinburgh, Edinburgh,  
EH9 3FD, Scotland, United Kingdom

<sup>2)</sup> Department of Bionanoscience, Kavli Institute of Nanoscience Delft,  
Delft University of Technology, Van der Maasweg 9,  
2629 HZ Delft, The Netherlands

We have developed an experimental method to perform interfacial rheology on liquid/liquid interfaces with no tool attached directly to the interface. This is achieved by shearing one of the liquid phases and measuring the interfacial response via confocal microscopy. Using this method we have measured steady shear material parameters such as the interfacial viscosity for fluid-like interfaces, and the interfacial elastic modulus for interfaces with solid-like behaviour. These measurements are in line with recent measurements made on similar systems using a conventional probe. Moreover, using our method we are able to measure lower interfacial viscosities than those that have previously been reported. This indirect method lends itself to microscopic structural analysis, as well as macroscopic rheological analysis, due to simultaneous microscopy. Our analysis shows that the interfacial behaviour is strongly dependent on the surface coverage and surface structure, and steady shear can have an irreversible effect on the structure of an interface.

## I. INTRODUCTION

Interfacial rheometry is essential when characterising systems with large interfacial area, such as emulsions or foams<sup>1,2</sup>. These systems are ubiquitous in industries such as pharmaceuticals, cosmetics and foodstuffs<sup>3-6</sup>. In order to probe the rheological properties, one can use shear rheology<sup>7-10</sup>, dilational rheology<sup>11-13</sup>, or simultaneously image the interface as shear is applied to connect the rheological properties to the interfacial microstructure<sup>14,15</sup>. In this work we focus on shear rheology, using an indirect probe with simultaneous imaging, in order to minimally disturb the interface before and during characterisation. We observe rheological properties consistent with previous measurements in the literature, and using this system we are able to simultaneously measure the interfacial structure and link this to the flow behaviour at the interface. Additionally, our setup has the advantages of being industrially relevant due to the indirect nature of the shear, and being able to measure lower interfacial viscosities than those that have been previously reported.

Previous work on interfacial shear rheology has used probes which directly attach to an oil/water or air/water interface, such as the magnetic rod interfacial stress rheometer<sup>16</sup>, or the double wall ring (DWR) geometry attached to a rotational rheometer<sup>7,14</sup>. These experimental setups are both based on the maximisation of the Boussinesq number<sup>2</sup> given in equation (1):

$$Bq = \frac{\eta_s}{\eta L}, \quad (1)$$

where  $\eta_s$  is the surface viscosity,  $\eta$  is the subphase viscosity and  $L$  is a characteristic length scale roughly equal

to the ratio of contact area to contact perimeter.  $Bq$  can be rewritten as the ratio of the surface drag force to the subphase drag force. In order to accurately measure the surface properties without unintentionally probing the subphase, this ratio must be maximised for the surface to contribute at least an order of magnitude more than the bulk. Of the two setups mentioned, the magnetic rod has the larger  $Bq$ , while both have a  $Bq$  an order of magnitude larger than that of a rotating disk, due to a much smaller  $L$ <sup>17</sup>. This maximisation of  $Bq$  can be considered as optimising the interface-to-bulk signal to noise ratio. Even though the magnetic rod set up has higher sensitivity, the DWR does have some advantages over the magnetic rod rheometer: it can be attached to a conventional rotational rheometer and has a larger dynamic range<sup>7</sup>.

In our work, we take a different approach which makes consideration of  $Bq$  less tangible as we have no contact area or contact perimeter. Rather than affixing a probe directly to the interface, we shear the upper phase, indirectly deforming the interface, and measure the response using confocal microscopy. We introduce an analogous  $Bq^*$  in § II C.

Our technique has two main advantages: (i) the interface we probe is purely a particle laden, liquid-liquid interface, with no large probe immersed therein, and (ii) this setup models general applications of these large interfacial area systems, where interfacial shear is applied indirectly by shearing the continuous phase. A clear example of this second point is in the application of skin creams, where upon application, the continuous phase is sheared which indirectly deforms the large area of interface present in the system. Notably, the equipment required to perform these measurements is relatively common. While we use confocal microscopy coupled to a stress-controlled rheometer, reflection or fluorescence microscopy coupled to a fixed rate motor should suffice. We show that our technique can be used to measure surfaces

<sup>a)</sup> Electronic mail: j.h.j.thijssen@ed.ac.uk

with lower viscosities than have been measured before, due to the inherent sensitivity of the technique arising from the response arising entirely from the interface itself. Finally, our setup lends itself to simultaneous structural analysis, which we show is key to understanding the rheological properties of a complex interface.

We investigate the efficacy of this method by studying a weakly interacting system of interfacially adsorbed colloidal particles. This system has been studied previously, looking into its interfacial rheology using a direct probing technique<sup>10</sup>, and considering the interparticle interactions of the interfacial colloidal particles<sup>18</sup>.

## II. MATERIALS AND METHODS

### A. Materials

Distilled and deionized (18 M $\Omega$ cm) water was used as the subphase and *n*-dodecane (Acros organics, 99% pure) was used as the upper phase. Prior to use, the *n*-dodecane was filtered three times through a column of alumina (Sigma-Aldrich, activated) to remove polar impurities following a standard procedure<sup>19</sup>.

Poly(methyl methacrylate) (PMMA) particles, stabilized by poly(lauryl methacrylate) (PLMA) were used, synthesised following<sup>20</sup>. These were labelled with fluorescent dye 4-chloro-7-nitrobenzo-2-oxa-1,3-diazol (NBD) in order to allow visualisation with confocal microscopy. The particles were sized by static light scattering (SLS) and found to have a diameter of 3.0  $\mu$ m with a polydispersity of 5%. Particles were cleaned by repeated centrifugation (5 $\times$ ) in *n*-hexane followed by repeated centrifugation (5 $\times$ ) in *n*-dodecane. The particles were kept as a dispersion in *n*-dodecane and sonicated for 30 minutes before dilution, followed by a further 30 minutes of sonication before use to minimise the number of aggregates in bulk.

### B. Methods

Interfaces were prepared in a custom made polytetrafluoroethylene (PTFE) cup with an aluminium ring insert to pin a flat interface. Fig. 1(a) shows a schematic representation of the cup. The cup's inner radius ( $r_c$ ) is 21 mm, the aluminium ring's inner radius ( $r_r$ ) is 10 mm. The aluminium ring has a height ( $h_r$ ) of 3 mm.

The PTFE cup was filled with water up to the roughened, pinning edge of the aluminium ring such that the depth of water was 3 mm. The edge was roughened manually using silicon carbide sandpaper. 3 ml of 0.005vol-% dispersion was carefully pipetted on to the interface and the interface was left to equilibrate for at least 1 hour. This procedure is calculated to give a depth of the oil phase ( $h_o$ ) of 2.165 mm.

A 25 mm diameter parallel plate geometry (Anton Paar PP25/S) was used with an Anton Paar MCR301

rheometer. The geometry was attached to the oil/air interface in the centre of the PTFE cup. Fixed rotation speeds,  $\omega$ , were applied to the geometry for 2 minutes before a further 30 s period of fixing the rotation of the rheometer to 0 to ensure the rheometer head stops moving. This protocol is summarised in Fig. 1(b) with the along with the confocal recording and measurement period.

Using a similar rheoimaging setup described by Besseling *et al.*<sup>21</sup> (although our rheometer setup lies directly on top of the confocal providing greater stability), rheometry was conducted while the interface was simultaneously imaged using a Leica SP8 confocal microscope with a 10 $\times$ , 0.3 NA air immersion objective. The imaging setup was such that the motion of the interface under shear was horizontally oriented. Velocimetry of the confocal images was performed using C code written in house. This splits the images into 10 equally spaced bands. Each band is correlated with the previous image at various horizontal offsets. The distance moved between that frame and the previous is then the horizontal offset which maximises this correlation.

The interfacial strain rate is calculated as  $\frac{v}{r_{out}}$ , where  $v$  is the measured velocity of the interface and  $r_{out}$  is the distance from the measurement to the outer, pinned wall. The velocity is measured by applying the velocimetry described above to the central 50% of the experiment, i.e. from 37.5 s to 112.5 s. To measure (elastic) strain at a high surface fraction, the size of the elastic recoil upon cessation of shear is found. This is converted to strain by dividing by  $r_{out}$ .

We use two methods for measuring surface fraction from magnified images: (i) we can measure the fraction of white pixels to total pixels after performing a thresholding procedure, or (ii) we can count the number of particles and use knowledge of particle size and image size to calculate surface fraction. In this work we refer to (i) as the pixel fraction method and (ii) as the particle counting method.

### C. Measuring Stress

To make meaningful statements on the rheological properties of the interface, we must first find the interfacial stress applied at the interface. It is well known that for a parallel plate setup, the stress is independent of the height through the sample upon reaching a steady state<sup>22</sup>. It can be shown that the timescale to reach steady state is on the order of 10 s for our setup<sup>22</sup>, for this reason we only measure interfacial strain rates at times  $> 30$  s. Considering the upper phase as a Newtonian fluid allows us to therefore find the stress on the interface from the upper fluid using the applied rotational speed of the geometry.

If the rheometer is rotated at a fixed angular velocity of  $\omega$  then the strain rate of the upper fluid at a radius  $r$

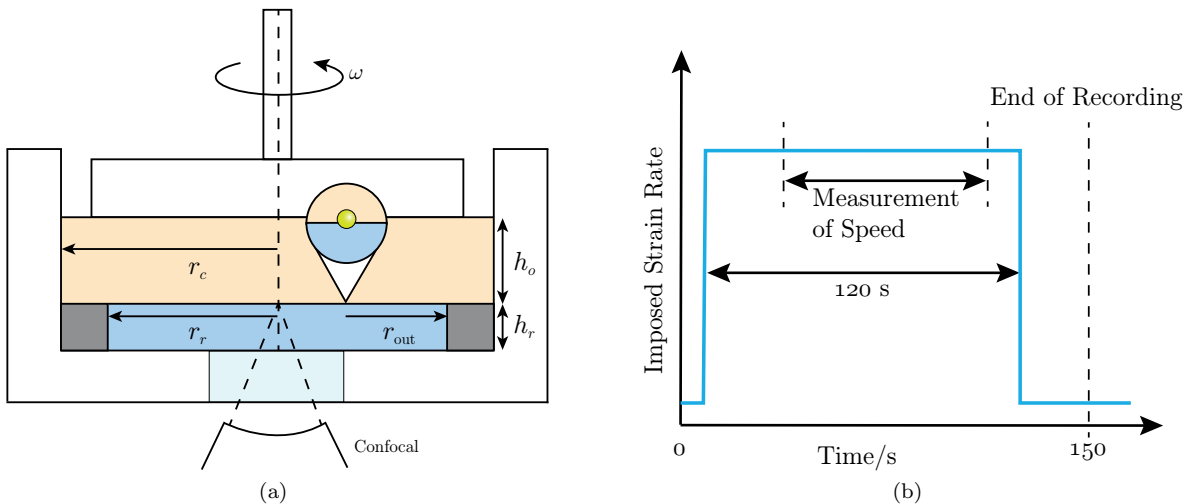


FIG. 1. (a) Schematic of the setup for performing indirect interfacial rheology using a parallel plate geometry attached to a stress controlled rheometer. The rheometer head is rotated at a fixed angular velocity,  $\omega$ . Imaging of the interface is done using a confocal microscope.  $r_c = 21$  mm,  $r_r = 10$  mm,  $h_r = 3$  mm, and  $h_o$  and  $\omega$  are varied for different experiments. Note,  $r_{out}$  is the radial distance from the measurement window to the outer, roughened edge of the aluminium ring. Note that the distances drawn are not to scale. (b) Experimental protocol highlighting start and end of shear, as well as the measurement window.

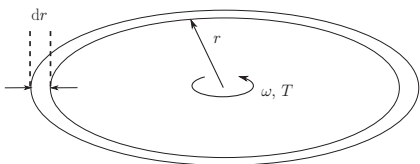


FIG. 2. Thin ring at oil/water interface. The interfacial stress can be found by considering the torque at the interface in terms of interfacial stress (see text for details).

(Fig. 2) of the parallel plate geometry is given by

$$\dot{\gamma} = \frac{\omega r}{h_o}, \quad (2)$$

where  $h_o$  is the depth of the oil phase. This definition relies on the interface having zero speed. This is therefore a first approximation if the speed of the geometry is much larger than the speed of the interface. If this is not the case then we can rescale  $\omega$  by the angular speed of the interface,  $\omega_i$ , at the radius  $r$ , leading to

$$\dot{\gamma} = \frac{(\omega - \omega_i)r}{h_o}. \quad (3)$$

The stress needed to induce this rotation is simply given by the product of strain rate with the bulk viscosity of the upper phase  $\eta_o$ , such that the stress is given by

$$\sigma = \frac{\eta_o(\omega - \omega_i)r}{h_o}. \quad (4)$$

To convert this bulk stress into an interfacial stress we

consider the torque applied from the bulk on an area element of a ring in the interface at  $r$  of width  $dr$ , Fig. 2.

We can write the torque element,  $dT$ , as a product of the force element,  $dF = \sigma dA$ , and the radius, where  $dA = 2\pi r dr$  is the area of the infinitesimal ring,

$$dT = \sigma 2\pi r^2 dr, \quad (5)$$

$$dT = 2\pi \frac{\eta_o(\omega - \omega_i)}{h_o} r^3 dr. \quad (6)$$

This torque then gives rise to the interfacial stress, where we can write a torque balance such that  $dT = T_s(r + dr) - T_s(r)$ , where  $T_s$  is the torque at the interface in terms of interfacial stress. This torque is the product of the perimeter,  $P$ , the interfacial stress,  $\sigma_s$  and the radius  $r$ ,

$$T_s(r) = P(r)\sigma_s(r)r. \quad (7)$$

$$\begin{aligned} dT &= T_s(r + dr) - T_s(r) \\ &= 2\pi(r + dr)(\sigma_s(r + dr))(r + dr) - 2\pi r \sigma_s(r)r \\ &= 2\pi r^2 \sigma_s(r + dr) + 4\pi r \sigma_s(r + dr)dr \\ &\quad - 2\pi r^2 \sigma_s(r), \end{aligned} \quad (8)$$

where terms in  $(dr)^2$  have been dropped. Equating equations (6) and (8) and rearranging terms leads to a first order ordinary differential equation

$$\frac{d\sigma_s}{dr} + \frac{2\sigma_s}{r} = \frac{\eta_o(\omega - \omega_i)}{h_o} r, \quad (9)$$

where upon taking  $dr \rightarrow 0$  we have equated  $\sigma_s(r+dr) = \sigma_s(r)$  in the second term of equation (8), equivalent to dropping terms of order  $dr^2$ .

Equation 9 can be readily solved to give

$$\sigma_s = \frac{\eta_o(\omega - \omega_i)}{4h_o} r^2 \quad (10)$$

if  $\frac{d\omega_i}{dr} \simeq 0$  (so there is no interfacial shear banding for example). It is evident this expression yields the correct dimensions for interfacial stress as Pa.m, as well as physically reasonable dependencies on viscosity, applied rotation, the height of the oil phase, and the radius. In order to vary the interfacial stress, we vary the rotation speed of the rheometer while observing the interface at a fixed radius. From a practical point of view, varying the rotation speed is simpler than varying  $r$ .

Finally, we need to ensure that we are measuring surface rather than bulk subphase properties. For setups with interfacial probes, this can be checked via the Boussinesq number (equation (1)), but this assumes a probe in contact with the interface. For our contactless setup, we instead consider a dimensionless number analogous to the Boussinesq number,

$$Bq^* = \frac{\eta_s h_o}{\eta_o r^2}, \quad (11)$$

where  $\eta_s$  is the interfacial viscosity. For the solution in equation (10) to be accurate,  $Bq^*$  must be  $\gg 1$ . We can consider the numerator here to be  $\eta_s r$  and the denominator to be  $\frac{\eta_o r^3}{h_o}$  which are, up to geometrical factors, the force per unit strain rate due to the interface and the force per unit strain rate due to the bulk respectively. Typical values for these parameters from previous work<sup>10</sup> on a similar system gives  $Bq^* \simeq 100$ . Given the above consideration,  $Bq^* \gg 1$  means that the interface dominates the rheological response in our set-up. We should be careful, however, when considering experiments done at lower surface fractions where we would expect a much lower surface viscosity and therefore a lower  $Bq^*$ .

### III. RESULTS AND DISCUSSION

#### A. Surface Coverage Measurement

It is important to understand the interfacial structure before looking at the rheological characteristics of the interface, as this plays a pivotal role in the rheological response<sup>15</sup>. We begin by considering the initial conditions, which include both surface structure and surface fraction,  $\phi$ . First, relatively high magnification images are analysed, the magnification level being a balance between individual particle resolution, which improves upon magnification, and statistics of particle counting, which decreases upon magnification. Two examples of initial conditions are shown in Fig. 3.

For Fig. 3(a), measurements of surface fraction via the pixel fraction and the particle counting methods give respectively 31.0% and 23.0% while for Fig. 3(b) these give respectively 56.7% and 46.1%. For conciseness, references to these experiments will only refer to the results from the pixel fraction method.

Note the significant difference in these measurements, highlighting flaws in one or both measurement methods. With perfect particle resolution, the particle counting method should yield the correct answer *for that particular region of the interface*, however, perfect particle resolution is rarely achieved for this system (especially at high  $\phi$ ), for instance because an aggregate of  $N$  particles could be mistaken for 1 particle. The pixel fraction method is also flawed in that it assumes a direct match between area of emitted light with area of the particle. This however is not true due to the point spread function, a question over whether the particles are exactly in the focal plane, and the brightness of the fluorophore itself, among other considerations. Comparing these images with other, similar images taken using the same imaging setup allows us to have an estimate for the surface fraction and certainly allows us to observe trends in flow behaviour as surface fraction changes, which we will discuss further on.

#### B. Structural Response to Shear

Image analyses reveal that the interfacial structure changes markedly upon shear, specifically above some critical shear rate. Initially the interfaces were quite well ordered, with some aggregation due to the high surface coverage and inherent attractive capillary or van der Waals forces. While capillary forces should be negligible, due to a vanishingly small Bond number and the use of spherical particles<sup>3</sup>, there will be a certain roughness to the particles and the effect of variable lengths of the steric stabiliser ‘‘hairs’’ on the particles’ surfaces may cause contact line undulations which lead to short range capillary attraction<sup>23,24</sup>. We see from images taken before and after shear is applied (figure 4) that the interface changes from a relatively homogeneous structure, with some small local variations in surface fraction, to an inhomogeneous structure with most particles forming one large aggregate percolating across the region imaged.

The structure in these images can also be analysed in a more quantitative manner in several ways, for example by looking at autocorrelation functions (ACF), region polydispersity, region size and Fourier analyses.

The most noticeable differences between the pre-shear ACF (figure 5(a)) and the post-shear ACF (figure 5(b)) are the brief oscillatory behaviour pre-shear, and the magnitude of the characteristic decay length. Short range oscillations in the ACF imply a degree of order, which can be seen from the real space image as, in general, particles are isolated from others, with the characteristic separation being able to be read from the ACF as the first maximum, occurring at  $7.3 \mu\text{m}$ . If we calculate the average

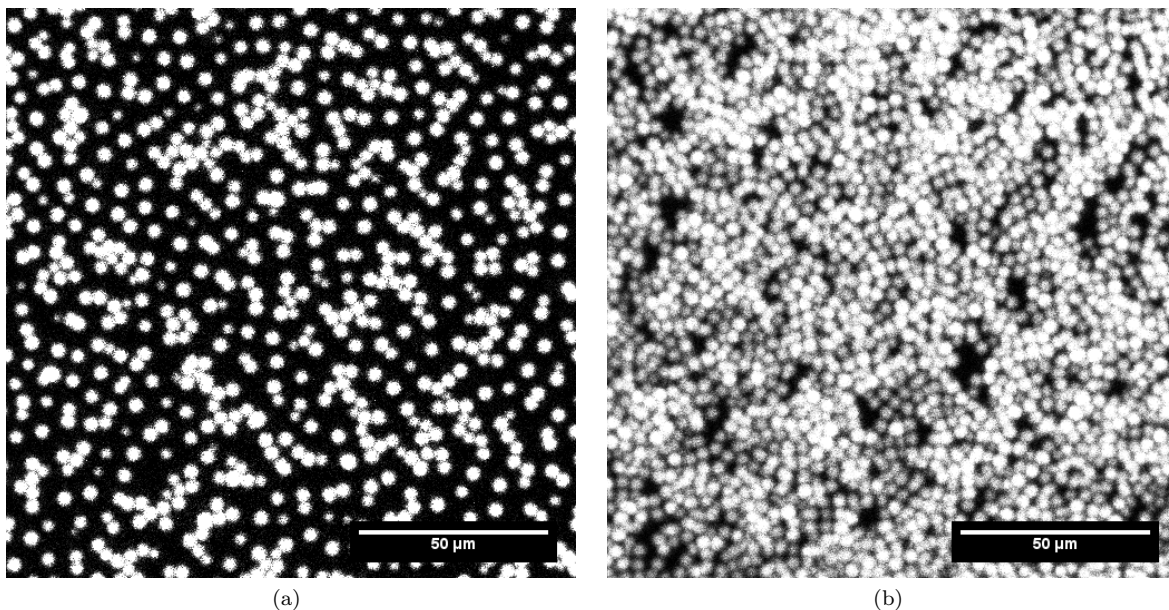


FIG. 3. Fluorescent confocal micrographs of PMMA-PLMA particles (white) at a water-oil interface at two initial conditions. (a) Surface fraction of 31.0%, (b) surface fraction of 56.7%, for details of surface fraction measurements see text. As well as a difference in surface fraction, the structure of these surfaces are markedly different, with (a) being dominantly separated particles with some aggregation, while (b) has a percolating structure but is not fully close packed.

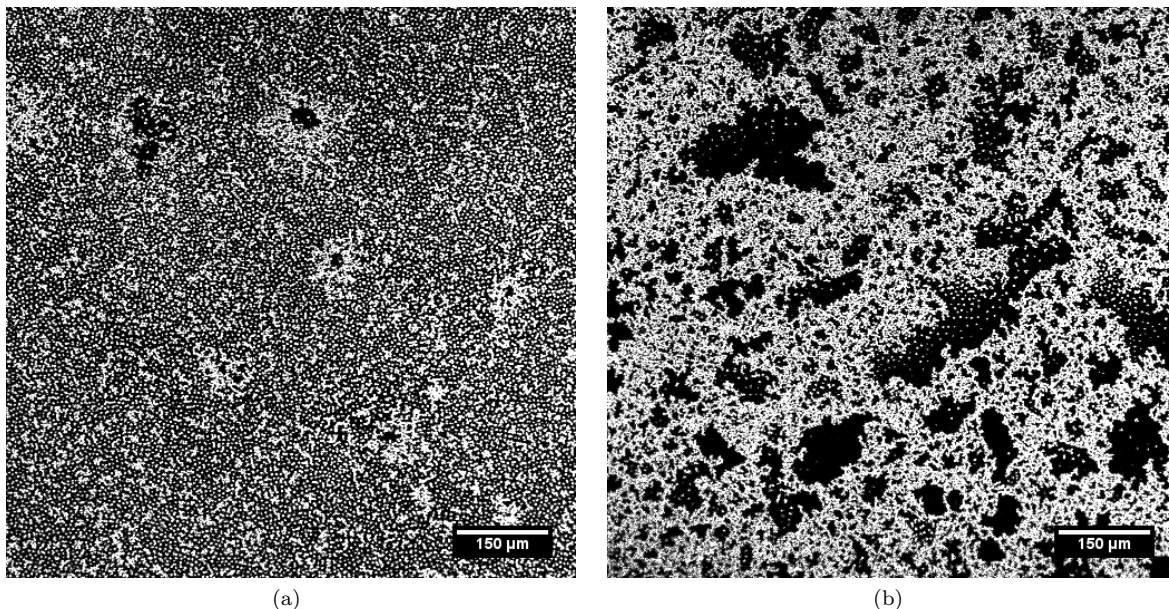


FIG. 4. Fluorescent confocal micrographs of PMMA-PLMA particles (white) at a water-oil interface (a) before and (b) after applying shears up to a rotation speed of the rheometer of 25.0 rev/min,  $\sigma_s = 0.02$  mPa.m. Comparing the two panels shows that the interfacial structure has changed markedly, becoming more heterogeneous after shear has been applied. The surface fraction determined from high magnification images of the same experiment is 31.0%.

interparticle separation based on the surface fraction we would find either  $4.8 \mu\text{m}$  or  $5.5 \mu\text{m}$  depending on which value of surface fraction is used (particle counting or area fraction). This discrepancy is caused by a relatively poor resolution in the image, each point in the ACF being sep-

arated by  $\sim 2 \mu\text{m}$ , and the lack of a hexagonal structure which is assumed for the estimate of average interparticle separation from surface fractions. In contrast, the post-shear ACF shows purely a decay, implying that the particles are commonly found in aggregates, or even a

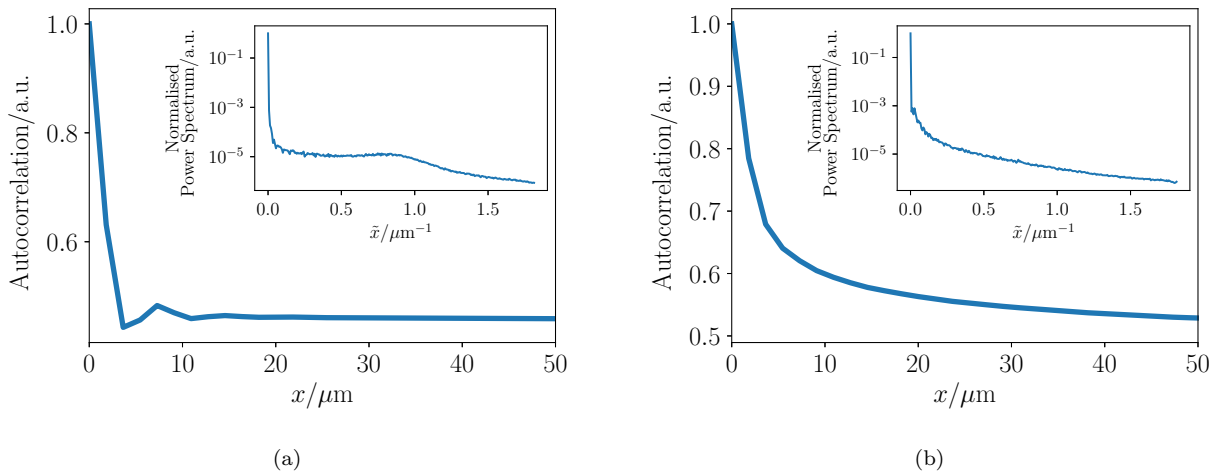


FIG. 5. Autocorrelation function and power spectrum (inset) of the images in figure 4 (a) preshear and (b) post shear.  $x$  is the separation of pixels in the correlation and  $\tilde{x}$  is the equivalent separation in reciprocal space. Note that  $x$  here represents the magnitude of the position vector  $\vec{x}$ .

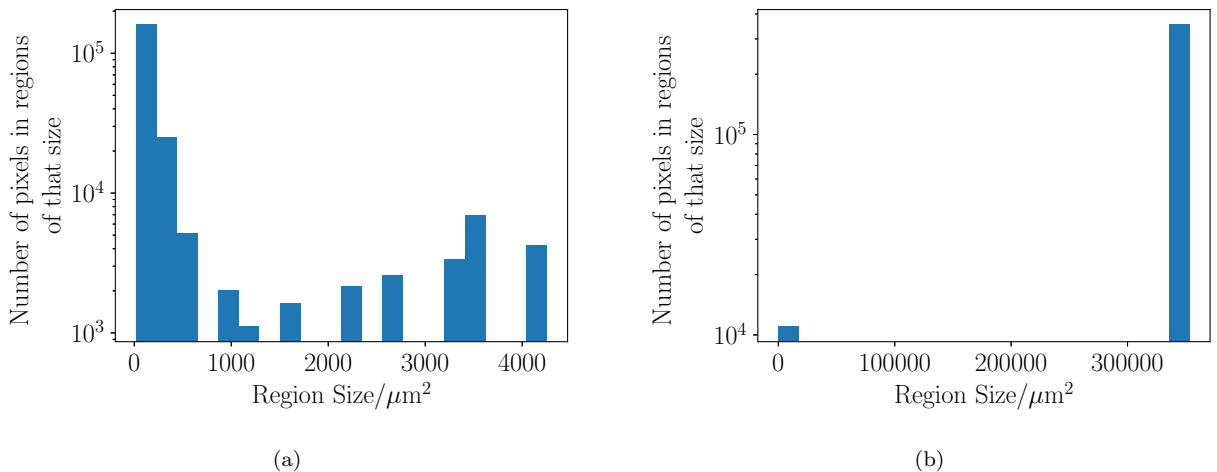


FIG. 6. Histograms for number of pixels in regions of a certain size for the images in Fig. 4 (a) pre shear and (b) post shear. The shapes of these indicate that in Fig. 4(a) there are many small regions showing little aggregation, while in Fig. 4(b) there is one large region with a few small regions, showing a large amount of aggregation.

single, percolating structure, as, no matter how far from one particle one checks, it is always more likely to find another particle there than at infinity<sup>25</sup>.

Power spectra calculated from interfacial micrographs also highlight the drastic change in structure after shear is applied. The change in behaviour of the pre-shear power spectrum (figure 5(a) inset) at  $\tilde{r} \simeq 1 \mu\text{m}^{-1}$  indicates a characteristic lengthscale in the image at around a separation of  $6.3 \mu\text{m}$ , in agreement with the ACF. Again, there is no such characteristic lengthscale post-shear (figure 5(b) inset), implying that there is no repeating structure.

In addition, region size analyses quantitatively show shear induced aggregation. These have been summarised

in a histogram of the number of pixels which are in a region of a specific size against that region size (figure 6). These histograms make clear the distinction between the two images. Pre-shear, we see pixels are mostly in very small regions, with some larger, aggregated regions. This contrasts the post-shear results, where almost every pixel is in a very large region, the bin being at  $344,000 \mu\text{m}^2$ , with the image size being  $932\mu\text{m} \times 932\mu\text{m}$  or  $868,624 \mu\text{m}^2$ , so 40% of the image is taken up by a single region. We can use these histograms to measure polydispersity, defined as the ratio of  $s$ , the standard deviation in cluster size, and  $\langle A \rangle$  the average cluster size<sup>10</sup>:

$$\mathcal{D} = \frac{s}{\langle A \rangle}. \quad (12)$$

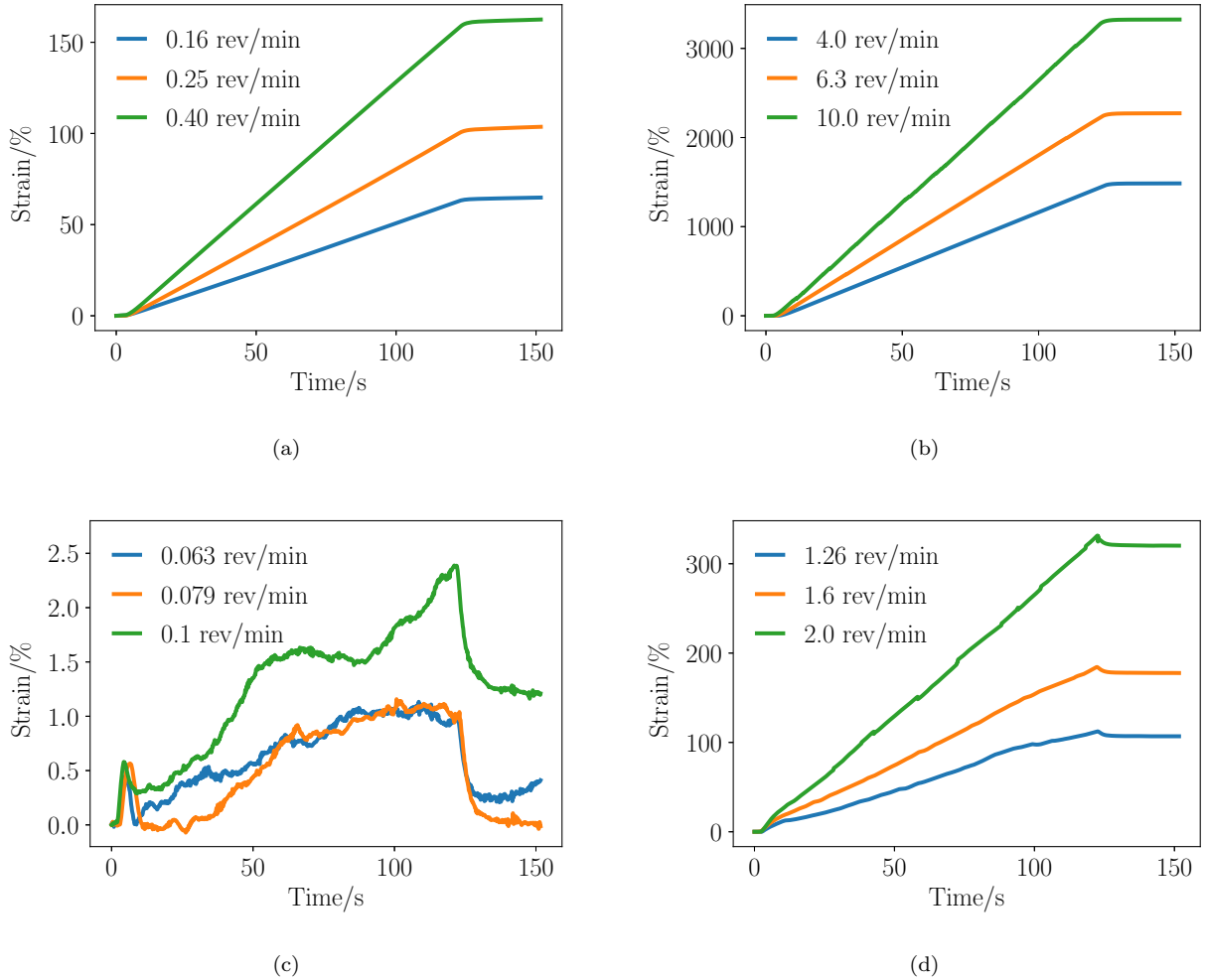


FIG. 7. Plots of strain vs time for experiments performed at  $\phi = 31.0\%$  at (a) low imposed rheometer rotation speed and (b) high imposed rheometer rotation speed, and  $\phi = 56.7\%$  at (c) low imposed rheometer rotation speed and (d) high imposed rheometer rotation speed. The rheometer rotation speeds are given in the legend of each figure. The plateaus in these plots, at 0 s and 130 s are due to video recording starting before and ending after the shear is applied. At the end of shear we sometimes observe motion (c), especially at low rotation rate, presumably due to thermal gradients or air flow - note however that the strain rates in this instance are small.

We find for the homogeneous, preshear surface,  $\mathcal{D} = 2.49$  while for post-shear we find  $\mathcal{D} = 13.5$ .

We have seen that applying shear leads to considerable aggregation in this system. In order for aggregation to occur the shear force must exceed the maximum repulsive force between these particles. It has been observed that these particles have an interaction that can be described by a repulsive screened Coulomb potential<sup>18</sup>. In order to overcome this repulsion we assume that they must overcome the maximum repulsive force, which for this potential is the point at which these particles are in contact, i.e.  $r = 3.0\mu\text{m}$ . This maximum force can be found to be  $9.88 \times 10^{-13}$  N, where we have rescaled the parameters from<sup>18</sup> as in this work we use larger particles. This force can then be converted to an interfacial stress by dividing by the particle diameter to give

a critical aggregation stress of  $3.3 \times 10^{-7}$  Pa.m. Experimentally, we found that aggregation occurs starting at a stress of  $2.6 \times 10^{-6}$  Pa.m, which is in reasonable agreement. This agreement between experiment and prediction lends confidence to the use of equation (10) when calculating interfacial stress in our unique geometry. In order to aggregate, the applied stress must also overcome the steric repulsion, however the steric barrier is considerably smaller (for a similar particle) than the electrostatic barrier<sup>18,26</sup>. Once these particles come into close contact, attractive capillary forces and/or van der Waals forces are large enough such that this is an irreversible state.

To summarise the interfacial structure section of our results, we have seen from these interfacial structure analyses that, upon shearing the interface there is a clear

transition from a relatively ordered state to a highly aggregated state which percolates across the field of view of the microscope. This behaviour is in line with estimates that show the energy input during shear can overcome the long-range repulsion between these particles, pushing the particles into an energy minimum which we argue is due to attractive capillary interactions and/or van der Waals interactions.

### C. Response to Shear

Having measured the surface structure, we now turn to interfacial rheology measurements. Strain vs time plots show a smooth flowing behaviour at the lower surface fraction (31%), with a constant strain rate over the duration of the shear being applied (figures 7(a) and 7(b)). As expected, at larger imposed shear rates from the rheometer a larger interfacial shear rate is measured in response. Note that, when shear starts the interface appears to immediately (within temporal resolution of the analysis method) begin flowing at a constant shear rate. Similarly, when the shear ends the interface immediately stops flowing. This implies that the response of the interface to shear in this regime is purely viscous with no measurable elastic behaviour.

At the higher surface fraction we observe markedly different behaviour, with elastic behaviour being evident from the strain vs time plots (figures 7(c) and 7(d)). Focussing on the low stress behaviour initially (figure 7(c)) an initial jump to a higher strain is observed, indicative of an elastic material. There is then some erratic motion in the direction of shear (i.e. the strain is always positive), indicating that there is some frustrated motion and rearrangements of the interfacial structure<sup>27</sup>. While the initial elastic response is difficult to measure precisely due to background noise in the flow, upon cessation of shear the interface clearly recoils, allowing the elastic strain to be readily measured<sup>28</sup>. This statement becomes even more apparent when looking at higher applied stresses, as at these large stresses the flowing behaviour completely dominates the strain response and the initial elastic jump is barely visible in the data. However, once the shear has been stopped, the elastic recoil is clear.

To quantify the rheological properties of these particle laden interfaces we plot stress vs strain rate to obtain a flow curve for each experiment at a different height of the oil phase. As expected, for relatively low surface coverages we observe a Newtonian response (figure 8). We can therefore attribute one constant value for interfacial viscosity for each oil phase height. These are comparable to what is measured using a magnetic rod interfacial rheometer on a similar system<sup>29</sup>.

We have performed repeats of these experiments while varying the thickness of the oil phase to test the robustness of our technique, observing some agreement across the three oil thicknesses tested (figure 8), suggesting that the height of the oil phase does not seem to have an ef-

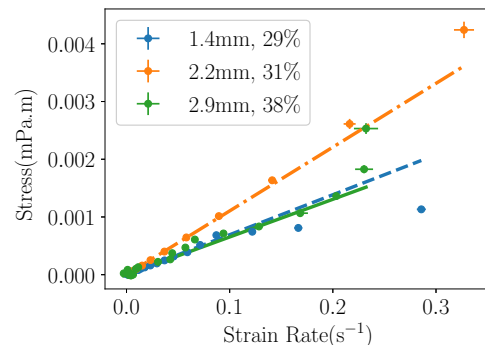


FIG. 8. Rheological behaviour of a particle laden interface at relatively low surface coverages (exact values given in legend). The three lines are measurements made at different oil layer thicknesses, which can be seen in the legend. Points are measured data, lines are fits to a linear model of constant viscosity. Interfacial viscosities are measured as  $6.9(3) \times 10^{-6}$  Pa.m.s (blue solid line),  $1.1(2) \times 10^{-5}$  Pa.m.s (orange dot-dashed line) and  $6.5(7) \times 10^{-6}$  Pa.m.s (green dashed line). Differences in interfacial viscosity arise due to different interfacial structures which can be quantified by polydispersity,  $\mathcal{D}$ .  $\mathcal{D}$  are measured to be 23.4 (blue solid line), 2.49 (orange dot-dashed line), and 24.7 (green dashed line). Note that the data points are logarithmically spaced such that points at lower strain rate appear to have a disproportionate affect on the fit when plotted on linear axes.

fect. However, there is some variation across the three measurements which the respective surface fractions we measure do not explain. Because of this we also measure the polydispersity at the interface using equation (12). For the data at 1.4 mm and 2.9 mm we find  $\mathcal{D} = 23.4$  and 24.7 respectively. Contrasting these numbers, we find for the data at 2.2 mm that  $\mathcal{D} = 2.49$ .

Both these measures of aggregation, combined with the values for the viscosity which were measured, indicate that the surface structure plays a significant role in the rheological properties of these interfaces. From the different values for  $\mathcal{D}$ , we can infer that a more aggregated interface leads to a lower viscosity. We finally note that, while the viscosities do vary for different oil thicknesses, the magnitudes of the stresses and strains are comparable across all thicknesses.

At higher  $\phi$  we observe a more complex rheological response, where the interface behaves as a yield stress fluid. Similarly to previously fitting a Newtonian, viscous response at lower  $\phi$ , at higher  $\phi$  we fit a linear dependence of the elastic strain response to the imposed shear stress in two regimes (figure 9(a)). This modelled Hookean behaviour gives us a shear modulus of  $6.7(3) \times 10^{-6}$  Pa.m at low strain and  $1.21(5) \times 10^{-5}$  Pa.m at high strain, consistent with previous measurements on a similar system<sup>10</sup>.

We fit the data to two straight lines as an approximation for the two regimes of elastic behaviour that we see both in the videos, and in the tracking (figure 7). This allowed us to measure one value for elastic modulus

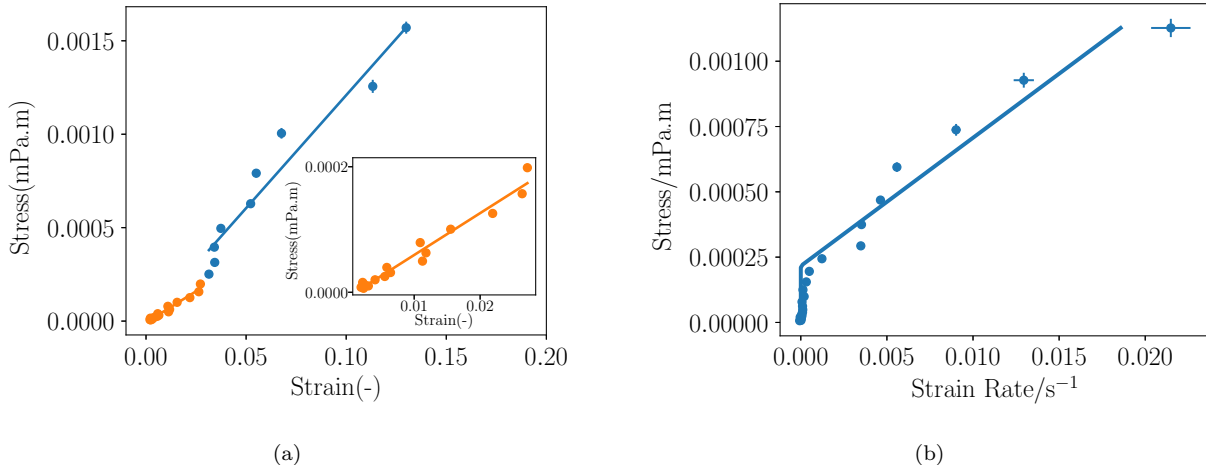


FIG. 9. Rheological behaviour of a dodecane-water interface laden with PMMA-PLMA particles at a surface fraction of 56.7%. (a) Elastic response of the interface to applied stress; the strain here is measured from the elastic recoil from velocimetry data. The data (points) have been fitted to a linear model (line) of stress vs. strain over two separate regimes at low strain and high strain; the inset is a zoomed in plot of the low strain behaviour. (b) Viscous response of the interface, i.e. after the initial elastic response but before the elastic recoil, with the data (points) fitted to a 2-dimensional Bingham fluid model (line).

at low strain and another at high strain. Both of these values are consistent with previous measurements in the literature<sup>10</sup>. However, we do note that there is a feature in the data in Fig. 9(a) around a strain of 0.03 which correlates almost exactly with the point at which we see the yielding behaviour in Fig. 9(b). We could therefore attribute (at least) two values of elastic modulus to this interface, one value before the interface yields and one after.

We also infer that this interface behaves as a yield stress fluid (figure 9(b)), as has been observed previously using the DWR geometry<sup>10</sup>. By fitting a simple piecewise function to these data, we can obtain both a yield stress and an effective viscosity. We model the interface as a Bingham fluid described by:

$$\begin{aligned} \dot{\gamma} &= 0 & : \sigma < \sigma_y \\ \sigma &= \sigma_y + \eta_s \dot{\gamma} & : \sigma \geq \sigma_y, \end{aligned} \quad (13)$$

where  $\sigma_y$  is the yield stress and  $\eta_s$  is an effective interfacial viscosity. Here we measure a yield stress of  $2.2(3) \times 10^{-7}$  Pa.m, an order of magnitude lower than the yield stress quoted in<sup>10</sup>, where the surface coverage is 78% in<sup>10</sup> and 56.7% for our measurements.

We feel that this is an appropriate model as the parameter which we are most interested in comparing to the literature is the yield stress. As noted, the yield stress we measure is an order of magnitude lower than the yield stress measured in<sup>10</sup>. However, here we measure a steady shear yield stress whereas the literature value is an oscillatory shear value, so a direct comparison of these is not necessarily appropriate<sup>30</sup>. Also, we are measuring at a surface fraction of 56.7%, while the surface fraction used in<sup>10</sup> was estimated at 78%. The smaller elastic modulus we measure would be expected considering this differ-

ence in surface fraction e.g.<sup>31,32</sup>. The effective interfacial viscosity that we measure,  $4.9(3) \times 10^{-5}$  Pa.m.s is, as expected, larger than what was measured at the lower surface fraction.

Our results, and the comparison to results on similar systems using the DWR<sup>10</sup> and the magnetic rod<sup>29</sup>, show that our setup represents a useful addition to the field of interfacial rheology. In comparable situations, our results are consistent with those from conventional probes, but crucially our setup allows us to measure viscosities at lower surface fractions than have been previously observed using the DWR. Using our system, we have linked the structural properties of the interface to the rheological response. In addition, our setup is industrially relevant for processing systems of large interfacial area, where the continuous phase is sheared, leading to indirect deformations of the interface.

#### IV. CONCLUSION

In this work, we have developed a novel method to perform interfacial rheology without an interfacial geometry. This allows us to probe interfaces in a less intrusive and a more industrially relevant manner than other, more direct methods. This method is relevant to applications where a system of large interfacial area is sheared, the shear being applied to the continuous phase and indirectly deforming the interface. We have demonstrated that we can measure rheological properties such as interfacial viscosity or yield stress depending on the surface fraction with this technique and the results align favourably with literature values. Our contactless setup allows us to measure interfacial viscosities at lower sur-

face fractions than have been previously observed using the DWR, owing to the high sensitivity achieved by having no probe attached directly to the interface. Additionally, while we use a confocal microscope to image the interface and a stress-controlled rheometer to apply a fixed rotation speed, the same results should be achievable using any fixed rate motor and reflection or fluorescence microscopy with sufficient resolution and frame rate. This enhances the applicability of this method as only relatively common equipment is required.

We have linked the rheological behaviour to the structural behaviour of interfaces with different initial conditions. At low surface coverage, the interface behaves as a two dimensional Newtonian fluid and is subject to aggregation above a certain shear threshold. At higher surface coverage the interface begins to behave as an elastic sheet with a measurable shear modulus, up to a yield stress where the interface begins to flow. Interestingly, we have observed that even above this yield stress, there is still some elastic behaviour present in the interface. In addition, we have shown that at low surface coverage, the interfacial structure has a strong effect on the rheology.

This work has focussed on the motion of the particles in the plane of the interface under steady shear. As the setup presented here does not have a probe attached to the liquid interface, the effect of the interface on how shear is propagated from the oil to the water phase can now be studied. This would facilitate observation of how the inside of an emulsion droplet is influenced by shear of the continuous phase, thereby greatly increasing the understanding and predictability of the flow behaviour of these systems, which are encountered ubiquitously in many formulation applications.

## V. ACKNOWLEDGMENTS

IM acknowledges studentship funding from the EP-SRC Centre for Doctoral Training in Condensed Matter Physics (CM-DTC, EP/L015110/1). The authors acknowledge A. B. Schofield for particle synthesis, J. A. Richards, R. O'Neill and R. Van Hooghten for useful discussions, J. Royer for assistance with the rheoimaging setup, and M. Hermes for the velocimetry code.

- <sup>1</sup>J. H. J. Thijssen and J. Vermant, "Interfacial rheology of model particles at liquid interfaces and its relation to (bicontinuous) Pickering emulsions," *Journal of Physics Condensed Matter* **30**, 023002 (2018).
- <sup>2</sup>G. G. Fuller and J. Vermant, "Complex Fluid-Fluid Interfaces: Rheology and Structure," *Annual Review of Chemical and Biomolecular Engineering* **3**, 519–543 (2012).
- <sup>3</sup>B. P. Binks and T. S. Horozov, eds., *Colloidal Particles at Liquid Interfaces* (Cambridge University Press, 2006).
- <sup>4</sup>J. W. Tavacoli, J. H. J. Thijssen, and P. S. Clegg, "CHAPTER 6. Bicontinuous Emulsions Stabilized by Colloidal Particles," in *Particle-Stabilized Emulsions and Colloids: Formation and Applications* (Royal Society of Chemistry, 2015) pp. 129–168.
- <sup>5</sup>F. Leal-Calderon and V. Schmitt, "Solid-stabilized emulsions," *Current Opinion in Colloid and Interface Science* **13**, 217–227 (2008).
- <sup>6</sup>T. N. Hunter, R. J. Pugh, G. V. Franks, and G. J. Jameson, "The role of particles in stabilising foams and emulsions," *Advances in Colloid and Interface Science* **137**, 57–81 (2008).
- <sup>7</sup>S. Vandebriel, A. Franck, G. G. Fuller, P. Moldenaers, and J. Vermant, "A double wall-ring geometry for interfacial shear rheometry," *Rheologica Acta* **49**, 131–144 (2010).
- <sup>8</sup>K. Masschaele, J. Franssaer, and J. Vermant, "Flow-induced structure in colloidal gels: direct visualization of model 2D suspensions," *Soft Matter* **7**, 7717 (2011).
- <sup>9</sup>N. C. Keim and P. E. Arratia, "Yielding and microstructure in a 2D jammed material under shear deformation," *Soft Matter* **9**, 6222 (2013).
- <sup>10</sup>R. Van Hooghten, V. E. Blair, A. Vananroye, A. B. Schofield, J. Vermant, and J. H. J. Thijssen, "Interfacial Rheology of Sterically Stabilized Colloids at Liquid Interfaces and Its Effect on the Stability of Pickering Emulsions," *Langmuir* **33**, 4107–4118 (2017).
- <sup>11</sup>B. Brugger, J. Vermant, and W. Richtering, "Interfacial layers of stimuli-responsive poly-(N-isopropylacrylamide-co-methacrylic acid) (PNIPAM-co-MAA) microgels characterized by interfacial rheology and compression isotherms," *Physical Chemistry Chemical Physics* **12**, 14573–14578 (2010).
- <sup>12</sup>S. Razavi, K. D. Cao, B. Lin, K. Y. C. Lee, R. S. Tu, and I. Kretzschmar, "Collapse of Particle-Laden Interfaces under Compression: Buckling vs Particle Expulsion," *Langmuir* **31**, 7764–7775 (2015).
- <sup>13</sup>V. Garbin, I. Jenkins, T. Sinno, J. C. Crocker, and K. J. Stebe, "Interactions and stress relaxation in monolayers of soft nanoparticles at fluid-fluid interfaces," *Physical Review Letters* **114**, 108301 (2015).
- <sup>14</sup>S. Barman and G. F. Christopher, "Simultaneous interfacial rheology and microstructure measurement of densely aggregated particle laden interfaces using a modified double wall ring interfacial rheometer," *Langmuir* **30**, 9752–9760 (2014).
- <sup>15</sup>S. Barman and G. F. Christopher, "Role of capillarity and microstructure on interfacial viscoelasticity of particle laden interfaces," *Journal of Rheology* **60**, 35–45 (2016).
- <sup>16</sup>C. F. Brooks, G. G. Fuller, C. W. Frank, and C. R. Robertson, "Interfacial stress rheometer to study rheological transitions in monolayers at the air-water interface," *Langmuir* **15**, 2450–2459 (1999).
- <sup>17</sup>K. Kim, S. Q. Choi, J. A. Zasadzinski, and T. M. Squires, "Interfacial microrheology of DPPC monolayers at the air-water interface," *Soft Matter* **7**, 7782–7789 (2011).
- <sup>18</sup>I. Muntz, F. Waggett, M. Hunter, A. B. Schofield, P. Bartlett, D. Marenduzzo, and J. H. J. Thijssen, "Interaction between Nearly Hard Colloidal Spheres at an Oil-Water Interface," *Physical Review Research* **2**, 023388 (2020).
- <sup>19</sup>A. Goebel and K. Lunkenheimer, "Interfacial tension of the water/n-alkane interface," *Langmuir* **13**, 369–372 (1997).
- <sup>20</sup>K. E. J. Barrett, ed., *Dispersion Polymerization in Organic Media* (New York: Wiley, 1974).
- <sup>21</sup>R. Besseling, L. Isa, E. R. Weeks, and W. C. K. Poon, "Quantitative imaging of colloidal flows," *Advances in Colloid and Interface Science* **146**, 1–17 (2009).
- <sup>22</sup>C. W. Macosko, *Rheology: Principles, Measurements, and Applications* (VCH, New York, 1994) p. 217.
- <sup>23</sup>D. Stamou, C. Duschl, and D. Johannsmann, "Long-range attraction between colloidal spheres at the air-water interface: The consequence of an irregular meniscus," *Physical Review E - Statistical Physics, Plasmas, Fluids, and Related Interdisciplinary Topics* **62**, 5263–5272 (2000).
- <sup>24</sup>R. Van Hooghten, L. Imperiali, V. Boeckx, R. Sharma, and J. Vermant, "Rough nanoparticles at the oil-water interfaces: Their structure, rheology and applications," *Soft Matter* **9**, 10791–10798 (2013).
- <sup>25</sup>Although the ACF should asymptotically level off at a constant value for a given area fraction of particles.
- <sup>26</sup>J. Mewis and J. Vermant, "Rheology of sterically stabilized dispersions and lattices," *Progress in Organic Coatings* **40**, 111–117

- (2000).
- <sup>27</sup>E. R. Weeks and D. A. Weitz, “Properties of Cage Rearrangements Observed near the Colloidal Glass Transition,” *Physical Review Letters* **89**, 095704 (2002).
- <sup>28</sup>L. Imperiali, K. H. Liao, C. Clasen, J. Fransaer, C. W. Macosko, and J. Vermant, “Interfacial rheology and structure of tiled graphene oxide sheets,” *Langmuir* **28**, 7990–8000 (2012).
- <sup>29</sup>S. Reynaert, P. Moldenaers, and J. Vermant, “Interfacial rheology of stable and weakly aggregated two-dimensional suspensions,” *Physical Chemistry Chemical Physics* **9**, 6463–6475 (2007).
- <sup>30</sup>T. G. Mason, J. Bibette, and D. A. Weitz, “Yielding and flow of monodisperse emulsions,” *Journal of Colloid and Interface Science* **179**, 439–448 (1996).
- <sup>31</sup>R. D. Groot and S. D. Stoyanov, “Equation of state of surface-adsorbing colloids,” *Soft Matter* **6**, 1682–1692 (2010).
- <sup>32</sup>J. P. Rane, V. Pauchard, A. Couzis, and S. Banerjee, “Interfacial rheology of asphaltene at oil-water interfaces and interpretation of the equation of state,” *Langmuir* **29**, 4750–4759 (2013).